Energy & Environmental Science

Cite this: *Energy Environ. Sci.*, 2012, **5**, 7081

www.rsc.org/ees

PAPER

Electrosynthesis, functional, and structural characterization of a water-oxidizing manganese oxide†

Ivelina Zaharieva,*[a] Petko Chernev,[a] Marcel Risch,‡[a] Katharina Klingan,[a] Mike Kohlhoff,[a] Anna Fischer[b] and Holger Dau*[a]

Received 23rd January 2012, Accepted 7th March 2012
DOI: 10.1039/c2ee21191b

In the sustainable production of non-fossil fuels, water oxidation is pivotal. Development of efficient catalysts based on manganese is desirable because this element is earth-abundant, inexpensive, and largely non-toxic. We report an electrodeposited Mn oxide (MnCat) that catalyzes electrochemical water oxidation at neutral pH at rates that approach the level needed for direct coupling to photoactive materials. By choice of the voltage protocol we could switch between electrodeposition of inactive Mn oxides (deposition at constant anodic potentials) and synthesis of the active MnCat (deposition by voltage-cycling protocols). Electron microscopy reveals that the MnCat consists of nanoparticles (100 nm) with complex fine-structure. X-ray spectroscopy reveals that the amorphous MnCat resembles the biological paragon, the water-splitting Mn_4Ca complex of photosynthesis, with respect to mean Mn oxidation state (*ca.* +3.8 in the MnCat) and central structural motifs. Yet the MnCat functions without calcium or other bivalent ions. Comparing the MnCat with electrodeposited Mn oxides inactive in water oxidation, we identify characteristics that likely are crucial for catalytic activity. In both inactive Mn oxides and active ones (MnCat), extensive di-μ-oxo bridging between Mn ions is observed. However in the MnCat, the voltage-cycling protocol resulted in formation of Mn^{III} sites and prevented formation of well-ordered and unreactive $Mn^{IV}O_2$. Structure–function relations in Mn-based water-oxidation catalysts and strategies to design catalytically active Mn-based materials are discussed. Knowledge-guided performance optimization of the MnCat could pave the road for its technological use.

[a]*Free University Berlin, Physics Department, Arnimallee 14, 14195 Berlin, Germany. E-mail: ivelina.zaharieva@fu-berlin.de; holger.dau@fu-berlin.de; Fax: +49 30 838 56299; Tel: +49 30 838 53581*
[b]*Technical University Berlin, Institute of Chemistry, Straße des 17. Juni, 10623 Berlin, Germany*

† Electronic supplementary information (ESI) available: Further details on the experimental techniques as well as on the protocols for electrodeposition of the Mn oxides, CVs for all discussed Mn oxides, electrochemical characterization of the MnCat, detection of O_2, stability tests, results from the attempt to activate the inactive Mn oxides by a voltage-cycling protocol, elemental analysis, and additional XAS data and simulations. See DOI: 10.1039/c2ee21191b

‡ Present address: Electrochemical Energy Laboratory, Massachusetts Institute of Technology, 77 Massachusetts Ave, Cambridge, MA 02139, USA.

Broader context

Threatening global climate changes and unsecured supply of fossil fuels call for a global transition toward sustainable energy-conversion systems. The storage of wind or solar energy by formation of energy-rich fuel molecules could play a central role in both transient storage of the intermittently provided energy and replacement of fossil fuels in the transportation sector. Whether hydrogen or a carbon-based fuel is the target, in any event the extraction of reducing equivalents and protons from water (that is, water oxidation) is pivotal. In search of water-oxidation catalysts that ultimately could play a role at a global scale, we and others are aiming at development of simple routes towards formation of Mn-based catalysts. Manganese excels by high availability and low toxicity; and in oxygenic photosynthesis, nature has demonstrated that a Mn-based catalyst can oxidize water efficiently. When aiming at an 'artificial leaf' with a Mn-based catalyst directly coupled to a solar-energy-converting material, the activity of the catalyst (per area) needs to cope with the incoming photon flux. Moreover the device design typically requires the use of benign synthesis and operation conditions, that is, temperatures close to room temperature and pH close to neutral. As an important first step, we report a simple protocol for electrodeposition of a Mn-oxide catalyst that fulfils the above requirements.

Introduction

Water oxidation is pivotal not only in powering life on earth by means of photosynthesis but also in technological systems for sustainable production of non-fossil fuels.[1] The vision of fuel production powered by solar energy has driven the rapid development of a research area today mostly described as 'artificial photosynthesis' or 'solar fuels'.[2–7] Whether production of molecular hydrogen or a carbon-based fuel is targeted, in any event the use of water as a source of reducing equivalents and protons is essential. We are aiming at electrosynthesis (electrodeposition) of a water-oxidation electrocatalyst that is based on the element also used in biological photosynthesis, that is, manganese.

In photosynthetic organisms, highly efficient water oxidation is catalyzed by a metal-oxo Mn_4Ca complex[8,9] embedded in a specific protein environment. Inspired by nature's catalyst for water oxidation, functional Mn-based molecular mimics[10–12] and Mn oxides[13–18] have been synthesized. Aside from fully molecular systems for fuel production which assume the presence of an electron acceptor, the water oxidation catalysts need to be connected to an electrode, photoanodes or photoactive semiconductor particles.[6,17,19,20] Grafting of molecular Mn complexes to surfaces may be possible.[21] Currently however, intricate synthesis routes and comparatively rapid ligand degradation disfavor their use as inexpensive and robust water oxidation catalysts in technological systems. Manganese oxides directly electrodeposited on electrodes represent an attractive option but standard deposition routes result in oxides of comparatively low catalytic activity (see Results section).

Recently, simple protocols to obtain electrodeposited catalysts based on Co[22] or Ni[23] oxides have been developed. Their low cost and operation under benign conditions (neutral pH range, room temperature) are favorable for realizing the concept of personalized energy[24] where inexpensive and simple devices replace the centralized large-scale energy conversion and distribution systems. In comparison to Co and Ni as the catalytic metal ion,[22,23] Mn is favored by:

(1) low price due to high abundance (Mn is the 10th most abundant element in the Earth crust[25,26]);

(2) low toxicity while Co and Ni are potentially carcinogenic;

(3) similarity to the Mn complex in photosynthesis rendering Mn-based electrocatalysts interesting functional models of the biological catalyst.

In the 70's and 80's, it was shown in several investigations that manganese oxides (*e.g.*, formed by thermal decomposition) can catalyze water oxidation, but mainly in alkaline solutions.[27–31] The active compounds in these first studies were described as mixtures of α-$Mn^{III}_2O_3$ and β-$Mn^{IV}O_2$ (rutile structures)[27–29,31] or as $AMn^{IV}O_3$ (perovskite, A = La, Sr).[30,31] The current interest in water oxidation catalysts based on earth-abundant metals has stimulated researchers to explore in more detail the usage of Mn-based electrocatalysts for water oxidation.[5,17,20,32,33] The procedures for synthesis of the catalysts range from electrodeposition routes at constant potential (originally developed for Mn oxides designed for use in batteries)[20] through more intricate electrodeposition routes involving rotating electrodes and voltage-cycling protocols[17] to immobilization of pre-synthesized molecular or colloidal Mn-based catalysts on the electrode surface.[5,16,32] The resulting structures are mainly layered type Mn oxides,[20,32] but also Mn_2O_3 structures[16,17] and spinel (Mn_3O_4) structures[6,16,19] with water oxidation activity have been reported.

The goal of the present study is to pave the road for usage of electrodeposited Mn-based catalysts in water-splitting devices similar to the "artificial leaf" presented by Nocera and coworkers.[34] The catalysts need to support the current densities required for directly light-driven water oxidation, that is, 1 to 15 mA cm^{-2}. The typical technological design of an artificial-leaf device asks for catalyst deposition and operation under benign conditions (neutral pH domain and room temperature).

To match the incoming flux of solar energy, current densities below 1 mA cm^{-2} are clearly insufficient. Thus we use this current density level to discriminate between low-activity and high-activity catalysts. In the following, all catalysts with catalytic currents below 1 mA (at pH 7 and 1.45 V *vs.* NHE) are considered to be low-activity catalysts or, at very low current levels, to be an inactive material. (We note that the level for a high-activity catalysts depends on the envisioned application. In alkaline water-electrolysis at elevated temperatures, clearly higher current densities can be reached often exceeding 100 mA cm^{-2}.[35])

Anodic electrodeposition results in water-oxidizing Co- or Ni-based materials[22,23] which have been identified as oxides with extensive di-μ-oxo bridging between high-valent metal ions.[36–38] Initially the Co-oxide catalyst was considered to be a cobalt-phosphate catalyst[22] but also electrodeposition in various phosphate-free electrolytes has yielded active catalysts[39,40] of similar atomic structure.[40] For electrodeposition of Mn oxides, the use of phosphate buffer is hindered by the rapid precipitation of Mn so that alternative electrolytes have to be employed.

Herein we describe the results of a screening of protocols for electrodeposition of Mn oxides. We identify conditions for electrosynthesis of Mn oxides that feature superior catalytic activity at neutral pH. Manganese oxides that are highly active in water oxidation are compared to low-activity oxides. Insight into the Mn oxidation state and atomic structure of the amorphous oxides is obtained by X-ray absorption spectroscopy. Ultimately, we identify distinct structural features associated with the observed catalytic activity and discuss the options for design of novel protocols for electrodeposition of active materials.

Experimental

Electrodeposition of Mn oxides

The Mn oxides were electrodeposited from aqueous Mn^{2+} solution (0.5 mM $Mn^{II}(CH_3COO)_2 \cdot 4H_2O$ in de-ionized water, in 0.1 M $MgSO_4$ or in 0.1 M $Na(CH_3COO)/CH_3COOH$ buffer at pH 6) on an inert working electrode (glass coated with indium tin oxide, ITO, 8–12 Ω sq^{-1}, Sigma Aldrich). A standard three-electrode system was used with a platinum mesh as a counter electrode and a Hg/Hg_2SO_4 electrode (saturated) as a reference electrode. Herein, the indicated potentials are always referenced to the normal hydrogen electrode (*vs.* NHE). For Mn oxide deposition, *iR* compensation was not applied. In 0.1 M $MgSO_4$ electrolyte as well as in the acetate buffer, the electrolyte resistance between working and reference electrode was relatively low (50 Ω) so that also the difference between the nominal and the *iR*-corrected potential was small.

For electrodeposition in low-salt electrolyte (de-ionized water containing exclusively 0.5 mM Mn acetate), an electrolyte resistance of 4.1 kΩ was determined by impedance spectroscopy. At this high level of the solution resistance, a stable *iR*-compensation is problematic. Consequently when using a voltage-cycling protocol, the actual electrode potentials deviate significantly from the nominal potentials of the working electrode. When applying nominal potentials of −0.75 V and +2.15 V, the actual *iR*-corrected potential at the working electrode would be (depending on the actual currents) −0.5 to +0.25 and +1.2 to + 1.7 V, respectively. Further details and deposition protocols are given in the ESI, S-1A and Fig. S1–S4†.

Electrochemical characterization

The catalytic activity of the electrodeposited Mn oxides was tested in 0.1 M phosphate buffer (pH 7, adjusted with 0.1 M KH_2PO_4 and 0.1 M K_2HPO_4). For the test procedures the typical electrolyte resistance (incl. the electrode) was about 40 Ω; *iR* compensation at 80% was applied.

The Tafel plot was obtained as shown in Fig. S5a–S5d†. To investigate the pH dependence, chronopotentiometric measurements maintaining a preset current (3 μA cm^{-2}, 10 μA cm^{-2}, and 30 μA cm^{-2}) were performed.

For further details on electrochemical procedures, UV-vis spectroscopy, scanning electron microscopy (SEM), elemental analysis and detection of O_2 evolution see the ESI†.

X-ray absorption spectroscopy

XAS measurements were performed at the BESSY synchrotron radiation source operated by the Helmholtz-Zentrum Berlin. The measurements at the manganese *K*-edge were acquired at the KMC-1 bending-magnet beamline at 20 K in a cryostat (Oxford-Danfysik) with a liquid-helium flow system. The incident energy was adjusted using a double-crystal monochromator (Si-111). A 13 element windowless Ge detector (Ultra-LEGe detectors, Canberra) was used to measure the X-ray fluorescence emitted from the sample (Mn K_α line). Further details are given in the ESI, S-1E†.

Results

Electrodeposition at constant and alternating potentials: from inactive to active Mn oxides

First we investigated a set of protocols for anodic electrodeposition of Mn oxides at constant potential. Similar protocols have been used successfully for electrodeposition of Co- or Ni-based materials which catalyze water oxidation.[22,23]

For electrodeposition of Mn oxides at constant anode potential, 0.5 mM of Mn^{2+} ions in three types of aqueous solution were used: (1) de-ionized water, (2) electrolyte at high ionic strength (0.1 M $MgSO_4$), and (3) buffered electrolyte (0.1 M sodium acetate buffer, pH 6). Different deposition potentials ranging from 0.95 to 2.15 V were applied for 15 min. As a source of Mn^{2+} ions, 0.5 mM Mn(II) acetate tetrahydrate was used but other Mn(II) salts (sulfate, nitrate, chloride) result in formation of very similar catalysts, as judged from the respective electrochemical activity and atomic structure (ESI, Fig. S2 and S12e†).

The catalytic activity of each electrodeposited Mn oxide was assessed in 0.1 M phosphate buffer at pH 7.0 (Fig. 1). (This specific buffer system was chosen in order to facilitate direct comparison to electrodeposited Co oxides.[22,41]) Essentially the same CVs were detected when using 0.1 M $Na(CH_3COO)$/0.1 M CH_3COOH solution (carefully adjusted to pH 7) instead of the phosphate buffer. The electrolysis buffer did not contain any Mn ions to avoid further deposition of Mn ions on the electrode surface when applying positive potentials. Under these standardized buffer conditions, all Mn oxides obtained by electrodeposition at constant potential exhibited either low catalytic activity or were found to be virtually inactive (see ESI, Fig. S2†). The highest catalytic current densities of around 200 μA cm^{-2} at 1.45 V were observed for manganese oxides deposited in acetate buffer at potentials around 1.6 V. Aiming at current densities of 1 mA cm^{-2} or higher, we consider the level of 200 μA cm^{-2} as clearly too low for practical use.

Jaramillo and coworkers electrodeposited a Mn oxide by consecutive application of two different potentials (5 min at 1 V followed by deposition of 25 mC at 1.2 V) and recorded sizeable catalytic currents at pH 13.[20] Using the protocol of Jaramillo and coworkers for Mn-oxide electrodeposition in a deaerated solution, we find that, at neutral pH, the activity of this oxide is comparable to the activity of the best Mn oxide obtained in the experiments described above (Fig. 1) but still is low in comparison to the Mn oxides described further below.

In conclusion, none of the herein used protocols for electrodeposition of water-oxidizing Mn oxides at constant anode potential results in electrocatalysts of satisfactory catalytic activity. This contrasts starkly with analogous Co- and Ni-based water-oxidation catalysts where active catalysts are obtained by electrodeposition at constant potential in a variety of buffer systems,[22,23] including acetate buffer and unbuffered solutions.[40]

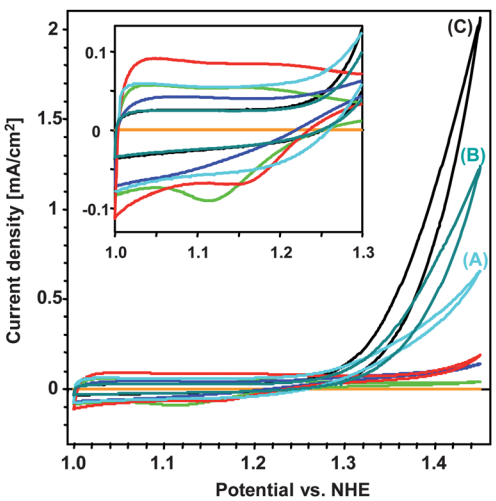

Fig. 1 Cyclic voltammograms (CVs) of electrodeposited Mn oxide films recorded in 0.1 M phosphate buffer at pH 7 (the second CV cycle is shown, sweep rate of 20 mV s^{-1}). Light blue, blue-green and black – MnCat deposited according to protocols A, B and C; green and blue – Mn oxide films deposited at constant potential of 1.35 V in de-ionized water and in 0.1 M acetate buffer, respectively; red – Mn catalyst deposited on FTO according to the procedure described in ref. 20; orange – blank ITO as a control.

Since electrodeposition at constant potential failed to produce high-activity oxides, we investigated more complex protocols involving periodic variation of the electrode potential. Three different electrodeposition protocols yielded a Mn-based water oxidation catalyst (MnCat) of superior catalytic activity (each comprising 25 cycles):

(A) For electrodeposition in 0.1 M $MgSO_4$ solution, the anode potential was changed stepwise between +1.4 V (for 29 s) and +0.25 V (for 29 s).

(B) For electrodeposition in de-ionized water, the anode potential was changed stepwise between +2.15 V (for 29 s) and −0.75 V (for 29 s).

(C) For electrodeposition in de-ionized water, the potential was cycled by continuous variation of the anode voltage between +2.15 V and −0.75 V (using triangular voltage variations as known from cyclic voltammetry; a sweep rate of 100 mV s^{-1}; 58 s per cycle).

The three voltage protocols are schematically shown in the ESI, Fig. S1†. The catalytic current is highest for protocol-C (cyclic sweeping in de-ionized water; Fig. 1, black line), intermediate for protocol-B and lowest for protocol-A. For all three protocols, the catalytic activity is superior to the highest activities obtained for deposition at constant potential. Notably, for protocol-C the catalytic current densities are comparable to the values reported for an electrodeposited Co oxide when tested in the same buffer system (0.1 M phosphate buffer, pH 7.0).

The electrolyte resistance in the de-ionized water containing exclusively 0.5 mM Mn acetate (protocols-B and C) was high (4.1 kΩ cm^{-1} as determined by electrochemical impedance spectroscopy) because only the highly diluted Mn acetate served as an electrolyte. Since no *iR* compensation was applied during electrodeposition, the actual anode potentials in protocols-B and C were clearly different from the nominal potentials. However the maximum and the minimum value of the actual electrode potential in B and C were comparable to the respective values used in protocol-A. For further details, see ESI, Fig. S1–S4†. We note that in the presence of 0.1 M $MgSO_4$, protocol-C does not result in formation of an active oxide. In protocol-A and B the actual anode potentials did not differ, but in protocol-A $MgSO_4$ was present at a concentration of 0.1 M. The comparison of protocol-A and B thus shows that high $MgSO_4$ concentrations reduce the catalytic activity, as also confirmed by systematic variation of the $MgSO_4$ concentration (data not shown). This observation implies that the electrolyte salt influences the catalytic activity and opens up the prospect of improvement of the catalysts by electrolyte variation.

In the following, a highly active (protocol-C) and a virtually inactive manganese oxide (deposited at constant potential) are compared structurally and functionally. We focus on the MnCat deposited according to protocol-C, not only because it is the most active catalysts, but also because the absence of redox-inert cations (*e.g.*, Mg^{2+}, Ca^{2+}, K^+, Na^+) simplifies the discussion of its atomic structure. The high-activity MnCat will be compared to a virtually inactive film deposited from an aqueous solution of 0.5 mM Mn acetate at a constant potential of +1.35 V. For both MnCat and the chosen inactive oxide, similar amounts of Mn, namely 4.4 μg cm^{-2} (80 nmol cm^{-2}) and 5.4 μg cm^{-2} (98 nmol cm^{-2}), respectively, were deposited on the working electrode, as determined by total reflection X-ray fluorescence (TXRF, see ESI, S-11†).

Functional characterization

To track the oxidation state changes of the Mn ions, we used UV-vis spectroscopy. Applying different oxidizing potentials to an already formed film in Mn^{2+}-free phosphate buffer, we did not observe significant change of the spectral shape, but an overall increase in extinction for an increase in potential (Fig. 2). Since at higher potentials oxidation of Mn ions is expected, we assume that the absorption increase reflects an increase in the average Mn oxidation state. Interestingly, we do not detect any bleaching. Thus we conclude that the extinction of the less oxidized form of the Mn oxide is clearly lower than for the oxidized form. Based on this assumption, we are using the extinction recorded at a fixed wavelength (450 nm, indicated with an arrow in Fig. 2B) to track qualitatively Mn oxidation-state changes (Fig. 3, insets). Recently a similar approach has been described for tracking Mn oxidation state changes in a birnessite-type Mn oxide grafted on an electrode.[42]

Fig. 3 facilitates the comparison of the current density ($I = dQ/dt$, per cm^2) and the first derivative of the absorption (dA_{450}/dt). In the CV of the active MnCat between 0.45 V and 1.2 V, the appropriately normalized derivative of the absorption signal follows the current closely (Fig. 3A). Current and absorption derivative imply a pseudocapacitive behavior which is explainable by the accumulation of redox equivalents and resembles the behavior of Mn oxides designed for use in batteries.[43,44] Integration of the reductive (negative) current (from Fig. 3) indicates that between 0.45 V and 1.2 V a sizeable fraction, that is, about 37% of the Mn ions change their oxidation state by one equivalent. At 1.2 V however, the two signals (I and dA_{450}/dt) split indicating the onset of the catalytic wave. This catalytic wave is

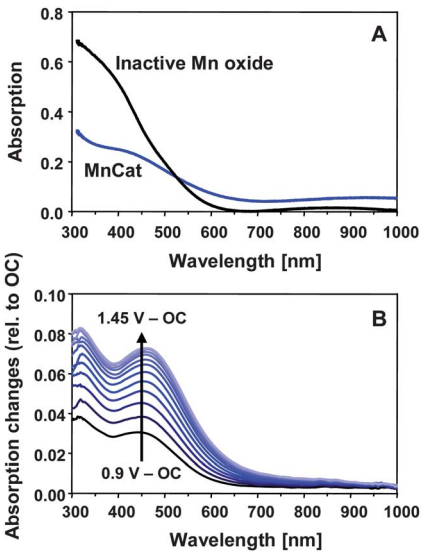

Fig. 2 (A) UV-vis absorption spectra of the MnCat and the inactive Mn oxide in dried state. (B) Difference spectra of the MnCat obtained by subtracting the spectrum recorded in phosphate buffer (pH 7) without any potential applied (open circuit condition, OC) from the spectra recorded in phosphate buffer at different potentials. In B, each potential was applied for 3 min prior to recording the corresponding spectrum. (The difference in working-electrode potential between the presented spectra is 0.05 V.)

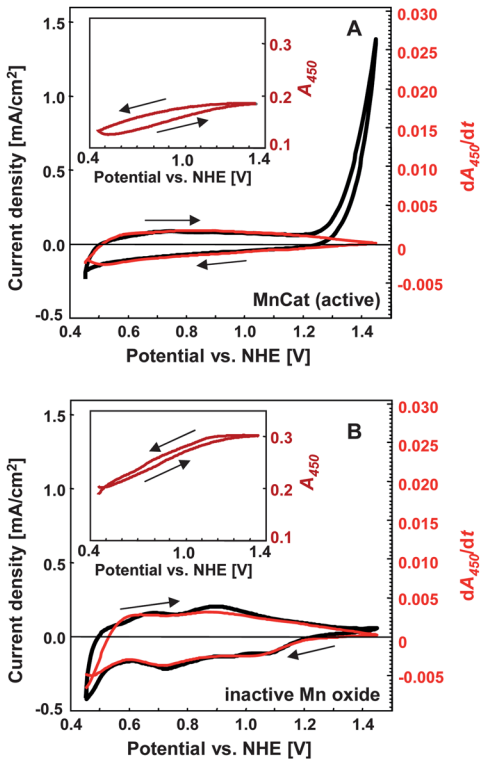

Fig. 3 Cyclic voltammograms (CVs) of electro-deposited Mn films, which are active (A) or inactive (B) in water oxidation (sweep rate 20 mV s^{-1}, second scan). The electrolyte was 0.1 M phosphate buffer (pH 7.0, Mn^{2+}-free buffer). Both the current (black line) and the absorption at 450 nm (dark red line in the inset) were recorded. The derivative of the absorption reflects the current flow assignable to changes in the Mn oxidation state (red lines in the main panels). Note the extended potential range in comparison to Fig. 1 (lower limit of +0.45 V *versus* 0.9 V in Fig. 1). At low electrode potentials, partial dissolution of the oxide film may occur likely explaining the lower catalytic current in comparison to CV data shown in Fig. 1.

lacking in the inactive Mn film (Fig. 3B), in which, surprisingly, the accumulation of redox equivalents occurs even at an enhanced level (oxidation state changes of 63% of the Mn ions). In the inactive film, at least two redox transitions with midpoint potentials of about 0.8 V and 1.15 V are discernible, possibly assignable to Mn^{II}–Mn^{III} and Mn^{III}–Mn^{IV} transitions. In the active MnCat separate redox transitions are not readily resolved, likely explainable by extreme broadening of these redox transitions by electronic interactions of Mn sites in the amorphous material.[45,46]

To verify that the current that is observed at higher potentials results from catalytic water oxidation and O_2 formation, the O_2-evolution rate of the MnCat was monitored in parallel in Mn^{2+}-free electrolyte. The O_2 evolution was detected with a Clark-type electrode at different (steady-state) potentials and during the CV (see ESI, S-6†). For voltages exceeding 1.2 V, we detected O_2 formation at a level that corresponds to the respective steady-state current. The rate of O_2-formation predicted from the electrical current (at 1.4 V, 2.56 μmol O_2 h^{-1} cm^{-2}) was only slightly higher than the rate detected by the Clark electrode (2.4 μmol O_2 h^{-1} cm^{-2}), suggesting that the Faradaic efficiency is close to 100%. The turnover frequency (TOF) at 1.35 V (*vs.* NHE) and room temperature was around 0.01 s^{-1} per deposited Mn ion and evolved O_2 molecule. At the same overpotential (and similar amounts of deposited metal ions), we determined a TOF of 0.017 s^{-1} for the Co-based electrocatalyst of ref. 22 and of 0.01 s^{-1} for the Ni-based electrocatalyst of ref. 23, both deposited at constant potential.

We studied the pH dependence of the anode potential required to reach a preset current level and determined a slope of about 60 mV per pH unit (Fig. 4A), as also reported for a Co-based electrocatalyst.[41] This behavior is explainable by formation of an intermediate state by Mn oxidation coupled to the release of one proton. This oxidation and deprotonation step is completed before onset of a relatively slow chemical step, the latter being largely insensitive to both the anode voltage and the buffer pH.[47]

The current–voltage relation (Tafel plot) of the MnCat at pH 7 in Mn-free phosphate buffer shows linearity of the log(*i*) *vs.* potential relation (Fig. 4B). For molecular catalysts with a reversible oxidation step prior to a turnover-limiting chemical step, a slope of about 59 mV per decade ($2.3 \times RT/F$) is predicted. However, for the MnCat we determined a slope of about 80 mV per decade, suggesting that the interaction energy between various oxidation sites in the amorphous catalyst is significant and affects the potential dependence. The latter conjecture is in line with the CVs of Fig. 3, which suggest extreme broadening of the oxidation (or reduction) peaks explainable by strong interactions between oxidation sites.

The Tafel plot of Fig. 4B suggests an overpotential of 565 mV cm^{-2} at 0.5 mA cm^{-2} and of 590 mV at 1 mA cm^{-2}. The former value was verified in the chronopotentiometric experiment of Fig. S5d†. We note that these overpotentials are still high in comparison to values for catalysts based on precious metals. For example, for an electrodeposited Ir-based amorphous electrocatalyst recently an overpotential of only 200 mV (at 0.5 mA cm^{-2}) was reported.[48] For technological use, improvement of the MnCat to reduce the overpotential will be of high importance.

Structural characterization

Both the active and the inactive films were visually uniform and adhered well to the ITO substrate. To probe the morphology of

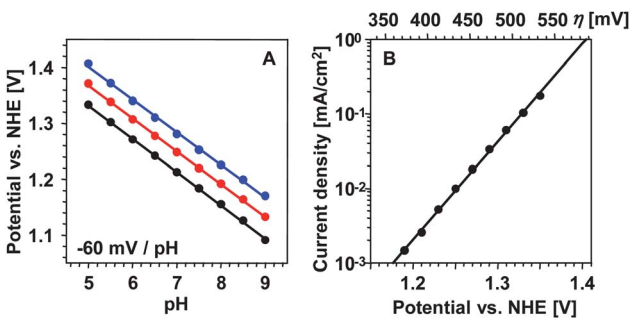

Fig. 4 (A) pH dependence of the electrode potential required for three anodic current densities (in 0.1 M phosphate buffer): 3 μA cm^{-2} – black, 10 μA cm^{-2} – red, and 30 μA cm^{-2} – blue. (B) Tafel plot of the Mn oxide catalyst in 0.1 M phosphate buffer at pH 7. The slope of the solid line corresponds to 76 mV per decade. The top scale provides the overpotential (η) relative to the equilibrium potential at pH 7. We note that also the data in panel-A suggests a (pH-independent) Tafel slope close to 80 mV per decade. For details see ESI, S-5†.

the electrodeposited material at the nanometre scale, we employed scanning electron microscopy (SEM) (Fig. 5). Both Mn films do not cover completely the surface of the electrode as the ITO layer is clearly visible between amorphous Mn oxide aggregates. The morphologies of the MnCat and the inactive film differ clearly. The active MnCat is composed of sand-rose like structures whereas the inactive one resembles a fluffy network. However, the surface area of the inactive oxide does not appear to be smaller than the surface area of the active oxide, as judged by visual inspection of the SEM image. This implies that the difference in catalytic activity is not explainable by a smaller surface area in the inactive oxide.

To elucidate the Mn oxidation state and the dominating structural motifs in the amorphous Mn oxides, we employed X-ray absorption spectroscopy (XAS).[49–51] The inset in Fig. 6 shows the X-ray absorption near-edge structure (XANES) spectrum of active and inactive Mn oxides, both frozen using the same protocol (after application of 1.35 V for 2 min in Mn-free phosphate buffer at pH 7; for details see ESI, S-1E†). Edge-rise energies are indicative of the mean oxidation state of manganese.[51] On the basis of a calibration employing simple Mn oxides, the average oxidation state of manganese in the active Mn film was estimated to be +3.8, while in the inactive film it was +4.0 (see ESI, Fig. S12a and S12b†). The shape of the XANES spectrum of the inactive Mn^{IV} oxide suggests the presence of a regular layered Mn oxide of the birnessite type[52,53] whereas the shoulders in the XANES of the active oxide point towards a more heterogeneous ligand environment.

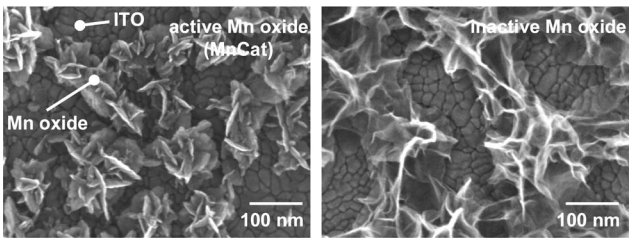

Fig. 5 SEM image of the electrodeposited Mn oxides. The active (MnCat, left) and inactive oxide (right), both do not form a continuous layer so that the nanostructure of the ITO substrate is visible.

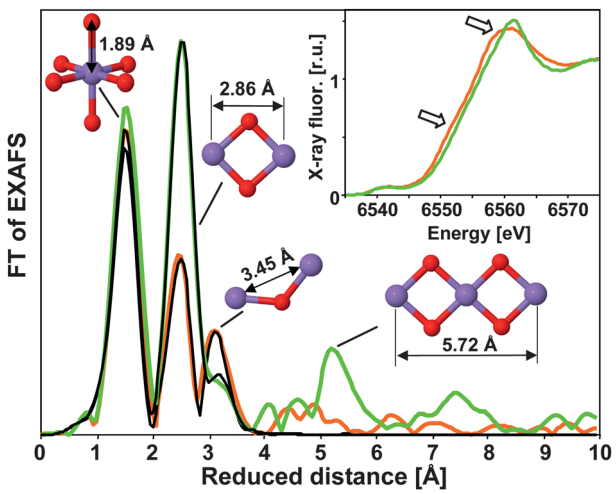

Fig. 6 X-ray absorption spectra of the MnCat (orange) and the inactive oxide (green). The edge region of the spectrum (XANES) is shown in the inset; the arrows mark shoulders in the MnCat spectrum. Each peak in the Fourier-transformed EXAFS spectra relates to a specific structural motif that is schematically depicted (O in red, Mn in purple). The spectra obtained by EXAFS simulations are shown as thin black lines (fit parameters in Table 1).

Fig. 6 shows the Fourier transforms (FTs) of the extended X-ray absorption fine structure (EXAFS) spectra. Ligation of Mn by ~6 oxygen atoms at a distance of 1.89 Å was determined by EXAFS simulations (Table 1), confirming the prevalence of $Mn^{IV}O_6$ in both the active and the inactive oxides. (The lower coordination number in the MnCat is explainable by the presence of Mn^{III}–O distances that are elongated along the Jahn–Teller axis so that they are not covered by the herein used simulation approach.)

The second prominent FT peak corresponds to a Mn–Mn distance of 2.86 Å, typical for di-μ-oxo bridging between Mn^{IV} ions as found in the birnessite-type of layered Mn oxides.[52–54] In a perfectly ordered layer formed from edge-sharing Mn octahedra (that is, di-μ-oxo bridging), for each Mn there are 6 neighboring Mn ions at 2.86 Å ($N_{2.86} = 6$), which is close to the situation in the inactive Mn film where about 4.3 Mn–Mn vectors of 2.86 Å length are detected (per X-ray absorbing Mn ion). A distance of 5.72 Å (2 × 2.86 Å) is expected in a well-ordered layered Mn oxide and is indeed visible in the inactive film. For the MnCat however, the number of 2.86 Å Mn–Mn vectors is clearly smaller, and instead a FT peak assignable to Mn–Mn vectors of 3.45 Å appears, pointing to the presence of mono-μ-oxo bridged Mn ions (corner-sharing octahedra).[52–54] (Additional EXAFS data and simulations are given in the ESI, S-12†.) We conclude that the inactive oxide resembles a layered $Mn^{IV}O_2$ with extensive di-μ-oxo bridging and significant long-range order. In clear contrast, the MnCat is a $Mn^{III/IV}$ oxide with a comparable number of di-μ-oxo and mono-μ-oxo bridges. Any long-range order is lacking in the MnCat.

The various protocols used for deposition at constant potential result in inactive oxides with XANES and EXAFS spectra resembling closely the spectra of the inactive Mn oxide shown in Fig. 6, suggesting largely identical oxidation-state level and atomic structure (see ESI, Fig. S12f†). We also found that an inactive oxide deposited at constant potential was not transformed into an active MnCat by application of a voltage-cycling

Table 1 Parameters obtained by simulation of the k^3-weighted EXAFS spectra. The simulated spectra correspond to the Fourier-transformed EXAFS spectra shown in Fig. 6. The errors represent the 68% confidence interval of the respective fit parameter (N, coordination number; R, absorber-backscatter distance; σ, Debye–Waller parameter)

	N	R [Å]	σ [Å]
Active Mn oxide (MnCat)			
Mn–O	5.3 ± 0.2	1.89 ± 0.003	0.066 ± 0.003
Mn–Mn, di-μ-oxo	2.6 ± 0.3	2.86 ± 0.004	0.070 ± 0.004
Mn–Mn, mono-μ-oxo	2.5 ± 0.3	3.45 ± 0.01	0.070 ± 0.004
Inactive Mn oxide			
Mn–O	5.9 ± 0.3	1.89 ± 0.003	0.069 ± 0.003
Mn–Mn, di-μ-oxo	4.3 ± 0.3	2.86 ± 0.002	0.054 ± 0.003
Mn–Mn, mono-μ-oxo	1.2 ± 0.2	3.49 ± 0.01	0.054 ± 0.003

protocol (ESI, S-9†). For the active MnCat, variation of the electrode material, annealing at 90 °C, and prolonged application of a constant potential of 1.35 V (in Mn-free phosphate buffer for 2 h) did neither affect its oxidation state nor its atomic structure (ESI, Fig. S12d†).

For technological applications, long-term stability of the MnCat will be crucial. Currently the activity of the MnCat decreases significantly within minutes when operated as a water oxidation catalyst at +1.35 V (*vs.* NHE) in a Mn-free phosphate buffer (ESI, S-8†) probably explainable by partial dissolution of the oxide. The atomic structure, however, remains unchanged (ESI, S-12†). Calcination at 90 °C does not prevent this activity loss whereas the stability of the catalytic current is greatly improved if the Mn film is covered with Nafion (ESI, S-7 and S-8†). Further optimization toward increased stability or self-repair will be of high interest. Grafting of Mn nanoparticles on a mesoporous scaffold[5,16] or coverage with nafion membranes[32] may represent interesting routes toward improved stability of the herein reported MnCat.

Discussion

Electrodeposition of a water-oxidizing Mn oxide

Searching for an efficient protocol for formation of a Mn-based water oxidation catalyst, we performed a screening of conditions for electrodeposition of Mn oxides. At sufficiently positive potential, Mn oxides are readily synthesized by anodic electrodeposition at constant potential at very low ion concentrations (only 0.5 mM of a Mn^{2+} salt) as well as in highly concentrated non-buffering (0.1 M $MgSO_4$) and buffering (0.1 M Na acetate) electrolytes. However the resulting oxides exhibit low catalytic activity only (or they are virtually inactive).

We report an electrodeposited Mn oxide with sizable catalytic activity at pH 7 in aqueous phosphate buffer, where the buffer ions (HPO_4^-) likely serve as an essential proton acceptor (unpublished results, see also ref. 39). However, the active material could *not* be prepared by electrodeposition at constant anode potential. The active MnCat was deposited using a protocol that involves recurrent oxidation-state changes of Mn ions caused by a voltage-cycling protocol.

Previously, thin films of nanostructured Mn oxide were deposited potentiostatically using a protocol that also involved a voltage-cycling protocol.[17] These films were found to be active for both oxygen reduction and water oxidation at pH 13, but activity at pH 7 was not verified. Moreover the synthesis protocol used in ref. 17 was not a mere electrodeposition and involved calcination at 480 °C, essentially excluding its use in the envisioned artificial-leaf system.

Structure–function relation

In the knowledge-guided search for more efficient catalysts, functional and structural characterization of the catalytically competent material is of high importance. Herein we show by EXAFS analyses that the formation of the high-activity MnCat and also of the inactive Mn oxide film involves electro-oxidation of dissolved Mn^{2+} and formation of di-μ-oxo bridges (most likely from water). The presence of high amount of di-μ-oxo bridged Mn ions (a Mn–Mn distance of 2.86 Å), a motif which also can be viewed as edge-sharing of MnO_6 octahedra, typically results in interconnected incomplete $Mn_3(\mu\text{-}O)_4$ or possibly also complete $Mn_4(\mu\text{-}O)_4$ cubanes, which are basic structural motifs in both the MnCat and the inactive Mn oxide. An additional feature observed only in the catalytically active MnCat is the high amount of mono-μ-oxo connected Mn ions (a Mn–Mn distance of about 3.4 Å).

The MnCat reported herein shares two characteristic metal–metal distances with the photosynthetic Mn_4Ca complex, namely a short Mn–Mn distance characteristic of di-μ-oxo bridging between Mn ions and a longer metal–metal distance around 3.4 Å.[9,55] (For a recent discussion of the structure of the biological catalyst, see ref. 56.) The Mn–Mn vectors assigned to di-μ-oxo bridging in the photosynthetic Mn complex are shorter than in the Mn oxides (around 2.72 Å)[9,55,57] explainable by μ_2-O bridging between only two Mn ions[58] as opposed to the prevalence of di-μ_3-O bridging (possibly also μ_2-OH) in the Mn oxides. (We note that in the MnCat, μ_2-oxo bridging is not excluded because a minor fraction of 2.7 Å Mn–Mn vectors of, *e.g.*, 10% would be irresolvable in the EXAFS analysis.) In the Mn_4Ca complex of oxygenic photosynthesis, the 3.3–3.5 Å vector detected by EXAFS spectroscopy relates to a Mn–Ca distance in a distorted $Mn_3Ca(\mu\text{-}O)_4$ cube.[56,59,60] In the synthetic MnCat however, neither Ca ions nor any other bivalent cation is present. It is conceivable that, in the MnCat, Mn ions attached by mono-μ-oxo bridges replace Ca with respect to its structural role in the photosynthetic Mn_4Ca complex and in Mn_2Ca-oxide particles.[61]

Bridging oxides likely are mechanistically pivotal in biological water oxidation.[8,62–64] Also in synthetic water-oxidizing oxides, extensive di-μ-oxo bridging between redox-active metal ions emerges as a key motif.[1] Di-μ-oxo bridging between first-row transition metals has been found to be the dominating structural motif for the Co-based electrocatalyst of Nocera and coworkers,[36,37] for the Ni-based electrocatalyst,[38] for colloidal Mn–Ca oxides,[61] and for the herein described MnCat. However, extensive di-μ-oxo bridging was observed also for the herein synthesized inactive Mn oxides indicating that, aside from extensive di-μ-oxo bridging, further aspects of the electronic structure are crucial for catalytic activity.

Both in the active MnCat and in β-$Mn^{IV}O_2$, a naturally occurring mineral,[65] a combination between extensive di-μ-oxo and mono-μ-oxo bridging is observed. However as opposed to the MnCat, the catalytic activity of β-$Mn^{IV}O_2$ is exceedingly low.[29] Well-ordered, microcrystalline Mn oxides generally may be largely inactive in water oxidation.[15,61] The prevalence of coordinatively saturated μ_{3-5}-oxo bonds and the absence of terminal coordination sites for water binding appear to preclude water-oxidation activity in both well ordered colloidal (see ref. 61) and electrodeposited Mn oxides. In conclusion, we propose that the relatively high extent of order in the Mn oxides deposited at constant potential is the cause for their comparatively low activity.

The anodic electrodeposition of Co and Ni oxides at constant potential results in a formation of catalytically active oxides with extensive di-μ-oxo bridging and largely without mono-μ-oxo bridging between the redox-active metal ions.[36,38] Similar mono-μ-oxo-free Mn oxides (resembling birnessites) can be formed by electrodeposition of Mn ions at constant potential (see Fig. 6 and ref. 20), but they are found to exhibit low activity only (Fig. 1 and

ESI, Fig. S2†). As opposed to Co^{IV} and Ni^{IV} dioxides, layered Mn^{IV} dioxides (*e.g.*, birnessites[26]) are readily formed and represent an energetically stable modification.[26] Thus we propose that there are two factors that render a $Mn^{IV}O_2$ a low-activity catalyst in the neutral pH domain. First, well-ordered $Mn^{IV}O_2$ layers result in the absence of readily (de)protonatable μ_2-O(H) groups and the lack of terminal water coordination sites.[1,9] Second, the energetic stability of reasonably well-ordered MnO_2 impedes water-oxidation catalysis.

We conclude that the electrodeposition of high-activity Mn-based catalyst asks for protocols that prevent formation of a stable $Mn^{IV}O_2$ modification. This can be realized, as demonstrated in our work, by cycling the electrode potential during electrodeposition. For electrodeposition with cycling potentials, the reduction of the $Mn^{IV}O_2$ oxide readily formed upon application of high potentials likely facilitates formation of low-order mixed-valent $Mn^{III/IV}$ oxide. A next step forward could be development of new protocols for electrodeposition of an active MnCat at constant potential, which may facilitate self-healing of the catalyst in the presence of Mn^{2+} ions, as reported for the Co-based electrocatalyst.[66] Aside from voltage cycling, it may be possible to develop further synthetic routes that prevent formation of a stable $Mn^{IV}O_2$ phase and enforce deposition of a fraction of Mn ions in a lower oxidation state. Illumination with visible or UV light is known to cause reduction of Mn^{IV} oxides;[32,67,68] illumination during electrodeposition may promote formation of an active MnCat. Moreover our screening of electrolytes has been by no means exhaustive. Future investigations may result in discovery of specific electrodeposition solutions for which the electrolyte ions become part of the Mn oxide and enforce formation of a low-order mixed-valent oxide also for electrodeposition at constant potential.

Conclusions

By choice of the voltage protocol, we could switch from electrosynthesis of a Mn oxide largely inactive in water oxidation to a high-activity oxide (MnCat). The herein presented MnCat is superior to previously published Mn-based catalysts as it catalyzes electrochemical water oxidation at neutral pH at rates that approach the level needed for direct coupling to photoactive materials. Even higher rates at lower overpotentials are desirable and represent an important target for future research, as is development and engineering of systems with long-term stability.

The voltage-cycling protocol resulted in an especially active Mn oxide, the MnCat. In clear contrast to the Co- and Ni-based catalysts, electrodeposition at constant potential resulted in an inactive Mn oxide. Active and inactive oxides differ in their nanostructure and at the atomic level. The latter difference appears to be decisive. The disorder in the atomic structure of the MnCat may facilitate μ_2-O(H) bridging and terminal ligation of water, and thereby catalytic activity. We believe that the functionally important disorder is jeopardized by the propensity of manganese to form at highly oxidizing potentials relatively well-ordered and stable (and thus inert) Mn^{IV} dioxides. The voltage-cycling protocol efficiently counteracts the formation of $Mn^{IV}O_2$. As opposed to Mn, electrodeposition of Co or Ni at constant potential results in formation of high-activity catalysts because even at especially oxidizing potentials, stable $Co^{IV}O_2$ and $Ni^{IV}O_2$ are not readily formed.

The herein presented results may pave the road for a knowledge-guided synthesis and optimization of water-oxidizing (electro)catalysts based on manganese, being earth-abundant and non-toxic and employed since billions of years for water oxidation in oxygenic photosynthesis.

Acknowledgements

We thank Dr M. Haumann (FU Berlin) for stimulating discussions. The XAS data were collected at the beamline KMC-1 of the BESSY, a synchrotron radiation source operated by the Helmholtz-Zentrum Berlin (HZB); we thank M. Mertin and Dr F. Schäfers for excellent technical support at KMC-1. Financial support by the Berlin Cluster of Excellence on Unifying Concepts in Catalysis (UniCat) and the European Union (7^{th} framework program, SOLAR-H2 consortium, #212508) is gratefully acknowledged.

Notes and references

1 H. Dau, C. Limberg, T. Reier, M. Risch, S. Roggan and P. Strasser, *ChemCatChem*, 2010, **2**, 724–761.
2 C. Herrero, B. Lassalle-Kaiser, W. Leibl, A. W. Rutherford and A. Aukauloo, *Coord. Chem. Rev.*, 2008, **252**, 456–468.
3 D. Gust, T. A. Moore and A. L. Moore, *Acc. Chem. Res.*, 2009, **42**, 1890–1898.
4 A. Magnuson, M. Anderlund, O. Johansson, P. Lindblad, R. Lomoth, T. Polivka, S. Ott, K. Stensjo, S. Styring, V. Sundstrom and L. Hammarstrom, *Acc. Chem. Res.*, 2009, **42**, 1899–1909.
5 F. Jiao and H. Frei, *Energy Environ. Sci.*, 2010, **3**, 1018–1027.
6 K. Maeda and K. Domen, *J. Phys. Chem. Lett.*, 2010, **1**, 2655–2661.
7 S. Styring, *Faraday Discuss.*, 2012, **155**, 357–376.
8 J. P. McEvoy and G. W. Brudvig, *Chem. Rev.*, 2006, **106**, 4455–4483.
9 H. Dau and M. Haumann, *Coord. Chem. Rev.*, 2008, **252**, 273–295.
10 J. Limburg, J. S. Vrettos, L. M. Liable-Sands, A. L. Rheingold, R. H. Crabtree and G. W. Brudvig, *Science*, 1999, **283**, 1524–1527.
11 M. Yagi and K. Narita, *J. Am. Chem. Soc.*, 2004, **126**, 8084–8085.
12 R. Brimblecombe, A. Koo, G. C. Dismukes, G. F. Swiegers and L. Spiccia, *J. Am. Chem. Soc.*, 2010, **132**, 2892–2894.
13 V. Y. Shafirovich, N. K. Khannanov and A. E. Shilov, *J. Inorg. Biochem.*, 1981, **15**, 113–129.
14 M. S. El-Deab, M. I. Awad, A. M. Mohammad and T. Ohsaka, *Electrochem. Commun.*, 2007, **9**, 2082–2087.
15 M. M. Najafpour, T. Ehrenberg, M. Wiechen and P. Kurz, *Angew. Chem., Int. Ed.*, 2010, **49**, 2233–2237.
16 F. Jiao and H. Frei, *Chem. Commun.*, 2010, **46**, 2920–2922.
17 Y. Gorlin and T. F. Jaramillo, *J. Am. Chem. Soc.*, 2010, **132**, 13612–13614.
18 M. M. Najafpour, S. Nayeri and B. Pashaei, *Dalton Trans.*, 2011, 9374–9378.
19 K. Maeda, A. Xiong, T. Yoshinaga, T. Ikeda, N. Sakamoto, T. Hisatomi, M. Takashima, D. Lu, M. Kanehara, T. Setoyama, T. Teranishi and K. Domen, *Angew. Chem., Int. Ed.*, 2010, **49**, 4096–4099.
20 B. A. Pinaud, Z. Chen, D. N. Abram and T. F. Jaramillo, *J. Phys. Chem. C*, 2011, **115**, 11830–11838.
21 L. Duan, L. Tong, Y. Xu and L. Sun, *Energy Environ. Sci.*, 2011, **4**, 3296–3313.
22 M. W. Kanan and D. G. Nocera, *Science*, 2008, **321**, 1072–1075.
23 M. Dincă, Y. Surendranath and D. G. Nocera, *Proc. Natl. Acad. Sci. U. S. A.*, 2010, **107**, 10337–10341.
24 D. G. Nocera, *Inorg. Chem.*, 2009, **48**, 10001–10017.
25 K. K. Turekian and K. H. Wedepohl, *Geol. Soc. Am. Bull.*, 1961, **72**, 175–192.
26 J. E. Post, *Proc. Natl. Acad. Sci. U. S. A.*, 1999, **96**, 3447–3454.
27 M. Morita, C. Iwakura and H. Tamura, *Electrochim. Acta*, 1977, **22**, 325–328.

28 M. Morita, C. Iwakura and H. Tamura, *Electrochim. Acta*, 1978, **23**, 331–335.
29 M. Morita, C. Iwakura and H. Tamura, *Electrochim. Acta*, 1979, **24**, 357–362.
30 Y. Matsumoto and E. Sato, *Electrochim. Acta*, 1979, **24**, 421–423.
31 Y. Matsumoto and E. Sato, *Mater. Chem. Phys.*, 1986, **14**, 397–426.
32 R. K. Hocking, R. Brimblecombe, L.-Y. Chang, A. Singh, M. H. Cheah, C. Glover, W. H. Casey and L. Spiccia, *Nat. Chem.*, 2011, **3**, 461–466.
33 M. Wiechen, H.-M. Berends and P. Kurz, *Dalton Trans.*, 2012, **41**, 21–31.
34 S. Y. Reece, J. A. Hamel, K. Sung, T. D. Jarvi, A. J. Esswein, J. J. H. Pijpers and D. G. Nocera, *Science*, 2011, **334**, 645–648.
35 D. Pletcher and X. H. Li, *Int. J. Hydrogen Energy*, 2011, **36**, 15089–15104.
36 M. Risch, V. Khare, I. Zaharieva, L. Gerencser, P. Chernev and H. Dau, *J. Am. Chem. Soc.*, 2009, **131**, 6936–6937.
37 M. W. Kanan, J. Yano, Y. Surendranath, M. Dinca, V. K. Yachandra and D. G. Nocera, *J. Am. Chem. Soc.*, 2010, **132**, 13692–13701.
38 M. Risch, K. Klingan, J. Heidkamp, D. Ehrenberg, P. Chernev, I. Zaharieva and H. Dau, *Chem. Commun.*, 2011, **47**, 11912–11914.
39 Y. Surendranath, M. Dinca and D. G. Nocera, *J. Am. Chem. Soc.*, 2009, **131**, 2615–2620.
40 M. Risch, K. Klingan, F. Ringleb, P. Chernev, I. Zaharieva, A. Fischer and H. Dau, *ChemSusChem*, 2012, **5**, 542–549.
41 Y. Surendranath, M. W. Kanan and D. G. Nocera, *J. Am. Chem. Soc.*, 2010, **132**, 16501–16509.
42 T. Takashima, K. Hashimoto and R. Nakamura, *J. Am. Chem. Soc.*, 2011, **134**, 1519–1527.
43 C.-C. Hu and T.-W. Tsou, *Electrochim. Acta*, 2002, **47**, 3523–3532.
44 K.-W. Nam, M. G. Kim and K.-B. Kim, *J. Phys. Chem. C*, 2007, **111**, 749–758.
45 T. Yamamoto, T. Maruyama, Z.-H. Zhou, T. Ito, T. Fukuda, Y. Yoneda, F. Begum, T. Ikeda and S. Sasaki, *J. Am. Chem. Soc.*, 1994, **116**, 4832–4845.
46 C. M. Julien, *Mater. Sci. Eng., R*, 2003, **40**, 47–102.
47 E. Gileadi, *Electrode Kinetics for Chemists, Chemical Engineers and Materials Scientists*, Wiley-VCH, New York, 1993.
48 J. D. Blakemore, N. D. Schley, G. W. Olack, C. D. Incarvito, G. W. Brudvig and R. H. Crabtree, *Chem. Sci.*, 2011, **2**, 94–98.
49 G. N. George, B. Hedman and K. O. Hodgson, *Nat. Struct. Biol.*, 1998, **5**, 645–647.
50 J. E. Penner-Hahn, *Coord. Chem. Rev.*, 1999, **190–192**, 1101–1123.
51 H. Dau, P. Liebisch and M. Haumann, *Anal. Bioanal. Chem.*, 2003, **376**, 562–583.
52 A.-C. Gaillot, D. Flot, V. A. Drits, A. Manceau, M. Burghammer and B. Lanson, *Chem. Mater.*, 2003, **15**, 4666–4678.
53 I. Saratovsky, P. G. Wightman, P. A. Pasten, J.-F. Gaillard and K. R. Poeppelmeier, *J. Am. Chem. Soc.*, 2006, **128**, 11188–11198.
54 T. G. Spiro, J. R. Bargar, G. Sposito and B. M. Tebo, *Acc. Chem. Res.*, 2010, **43**, 2–9.
55 V. K. Yachandra, K. Sauer and M. P. Klein, *Chem. Rev.*, 1996, **96**, 2927–2950.
56 A. Grundmeier and H. Dau, *Biochim. Biophys. Acta*, 2012, **1817**, 88–105.
57 V. K. Yachandra, R. D. Guiles, A. McDermott, R. D. Britt, S. L. Dexheimer, K. Sauer and M. P. Klein, *Biochim. Biophys. Acta*, 1986, **850**, 324–332.
58 H. Dau, P. Liebisch and M. Haumann, *Phys. Chem. Chem. Phys.*, 2004, **6**, 4781–4792.
59 R. M. Cinco, K. L. M. Holman, J. H. Robblee, J. Yano, S. A. Pizarro, E. Bellacchio, K. Sauer and V. K. Yachandra, *Biochemistry*, 2002, **41**, 12928–12933.
60 C. Müller, P. Liebisch, M. Barra, H. Dau and M. Haumann, *Phys. Scr., T*, 2005, **115**, 847–850.
61 I. Zaharieva, M. M. Najafpour, M. Wiechen, M. Haumann, P. Kurz and H. Dau, *Energy Environ. Sci.*, 2011, **4**, 2400–2408.
62 H. Dau, L. Iuzzolino and J. Dittmer, *Biochim. Biophys. Acta*, 2001, **1503**, 24–39.
63 H. Dau and M. Haumann, *Photosynth. Res.*, 2005, **84**, 325–331.
64 P. E. Siegbahn, *Chem.–Eur. J.*, 2008, **14**, 8290–8302.
65 R. W. G. Wyckoff, *Crystal Structures*, Interscience Publishers, New York, 2nd edn, 1963, pp. 239–444.
66 M. W. Kanan, Y. Surendranath and D. G. Nocera, *Chem. Soc. Rev.*, 2009, **38**, 109–114.
67 W. G. Sunda, S. A. Huntsman and G. R. Harvey, *Nature*, 1983, **301**, 234–236.
68 W. G. Sunda and S. A. Huntsman, *Mar. Chem.*, 1994, **46**, 133–152.